XI International Conference on Computational Plasticity. Fundamentals and Applications
COMPLAS XI
E. Oñate, D.R.J. Owen, D. Peric and B. Suárez (Eds)

FINITE DEFORMATION DAMAGE MODELLING IN CHALLENGING APPLICATIONS - FORMING LIMIT DIAGRAMS AND LIFE TIME ANALYSIS FOR A ROCKET THRUST CHAMBER

VIVIAN TINI*, IVAYLO N. VLADIMIROV*, YALIN KILICLAR* AND STEFANIE REESE*

*RWTH Aachen University
Institute of Applied Mechanics
Mies-van-der-Rohe Str. 1, D-52074 Aachen, Germany
e-mail: stefanie.reese@rwth-aachen.de, www.ifam.rwth-aachen.de

Key words: Finite Deformation Damage, Forming Limit Diagram at Fracture, Lifetime Analysis, Rocket Thrust Chamber

Abstract. This paper presents the coupling of a recently developed finite anisotropic elastoplastic constitutive model with isotropic ductile damage. The feasibility of the model for failure prediction purposes is presented in two challenging applications. The first one concerns the prediction of forming limit diagrams at fracture (FLDF) by means of finite element simulations of the so-called Nakajima stretching test. In the second application, the model is utilized in a thermomechanical analysis of a rocket combustion chamber segment. In both applications, the potential of the model for failure prediction purposes is discussed.

1 INTRODUCTION

In some engineering applications, such as in forming processes of metal sheets, it is common to have more than ten percent of plastic strain at failure. On applications involving polymers, failure can occur at a very large value of strain, i.e. a few hundred percent. In these cases, small strain damage formulations are no longer sufficient to provide a reliable failure prediction. For this purpose, a continuum damage formulation in the framework of finite deformations is necessary.

In this paper, the coupling of an anisotropic finite elastoplastic constitutive model with isotropic damage will be introduced. The complete derivation of the anisotropic elastoplastic model has been published recently [1]. The triple multiplicative split of the deformation gradient is performed to incorporate nonlinear kinematic hardening according

to the Armstrong-Frederick concept [2]. The most important steps of the derivation and the extension of the model to include isotropic damage will be presented in Section 2.

The model is implemented as a user subroutine UMAT into the Abaqus finite element analysis software. Upon successful numerical validations by means of a number of uniaxial, multiaxial, monotonic and cyclic loadings, the model is applied to challenging finite element simulations which will be described in Section 3 and Section 4.

In Section 3 the application of the model to generate forming limit diagrams at fracture (FLDF) will be discussed. The prediction of FLDF is especially important when forming is limited by fracture rather than necking. In cases where the strain path approaches equibiaxial stretching, ductile fracture due to void formation might be induced before the onset of localized necking. In such situations it is essential to predict the occurence of fracture. For this purpose, the simulation of the so-called Nakajima stretching test are performed. The results are used to generate the forming limit diagrams at fracture.

The second application concerns failure which occurs at the cooling channel wall of a rocket thrust chamber. The extreme thermomechanical loadings during the operation of the rocket lead to the thinning and bulging of the cooling channel wall, which eventually causes the so-called "dog house" failure mode [3]. A transient heat transfer analysis is performed to obtain the temperature history of the modelled chamber segment. Afterwards a series of static analyses is performed to obtain the stress-strain field as well as the cyclic evolution of the damage. The computation results show the potential of the model to predict the end shape of the cooling channel wall.

2 FINITE STRAIN DAMAGE MODELLING

This part will summarize the most important steps of the derivation of the anisotropic elastoplastic model and its coupling with an isotropic damage variable following the principle of strain equivalence as elaborated by Lemaitre [4].

The constitutive model uses the triple multiplicative decomposition of the deformation gradient $\mathbf{F} = \mathbf{F}_e \, \mathbf{F}_{p_e} \, \mathbf{F}_{p_i}$ into elastic ($\mathbf{F}_e$), plastic-elastic ($\mathbf{F}_{p_e}$) and plastic-inelastic ($\mathbf{F}_{p_i}$) parts. The additional multiplicative split of the plastic part of the deformation gradient into elastic and inelastic parts is performed for the modelling of nonlinear kinematic hardening according to the Armstrong-Frederick concept [2]. This split can be physically motivated by taking into account the dislocation-induced lattice rotations and stretches and local plastic deformations on the microscale.

Based on the principle of material objectivity and the concept of material isomorphism the Helmholtz free energy per unit volume can be written in the form

$$\psi = \psi_e \left(\mathbf{C}_e, D \right) + \psi_{kin} \left(\mathbf{C}_{p_e}, D \right) + \psi_{iso} \left(\kappa, D \right) \tag{1}$$

where $\mathbf{C}_e = \mathbf{F}_e^T \, \mathbf{F}_e = \mathbf{F}_p^{-T} \, \mathbf{C} \, \mathbf{F}_p^{-1}$ represents the elastic right Cauchy-Green deformation tensor and $\mathbf{C}_{p_e} = \mathbf{F}_{p_e}^T \, \mathbf{F}_{p_e} = \mathbf{F}_{p_i}^{-T} \, \mathbf{C}_p \, \mathbf{F}_{p_i}^{-1}$ the elastic part of the plastic right Cauchy-Green tensor. The first part ψ_e describes the macroscopic elastic material properties. The terms ψ_{kin} and ψ_{iso} represent the amounts of stored energy due to kinematic and

isotropic hardening, respectively. The variable κ refers to the accumulated plastic strain. The scalar D represents the isotropic ductile damage variable, where $D = 0$ holds for a virgin (undamaged) material point and $D = 1$ for a completely damaged material point.

The constitutive equations of the model are obtained from the derivation based on the Clausius-Duhem form of the second law of thermodynamics $-\dot{\psi} + \mathbf{S} \cdot \frac{1}{2}\dot{\mathbf{C}} \geq 0$. Inserting the Helmholtz free energy and differentiating with respect to time yields

$$-\left(\frac{\partial \psi_e}{\partial \mathbf{C}_e} \cdot \dot{\mathbf{C}}_e + \frac{\partial \psi_{kin}}{\partial \mathbf{C}_{p_e}} \cdot \dot{\mathbf{C}}_{p_e} + \frac{\partial \psi_{iso}}{\partial \kappa}\,\dot{\kappa} + \frac{\partial \psi}{\partial D}\,\dot{D}\right) + \mathbf{S} \cdot \frac{1}{2}\,\dot{\mathbf{C}} \geq 0 \tag{2}$$

The specific forms of the energy contributions ψ_e, ψ_{kin} and ψ_{iso} are given as $\psi_e = (1-D)\,\bar{\psi}_e$, $\psi_{kin} = (1-D)\,\bar{\psi}_{kin}$ and $\psi_{iso} = (1-D)\,\bar{\psi}_{iso}$, where

$$\bar{\psi}_e = \frac{\mu}{2}\,(\operatorname{tr}\mathbf{C}_e - 3) - \mu\,\ln\left(\sqrt{\det \mathbf{C}_e}\right) + \frac{\Lambda}{4}\,(\det \mathbf{C}_e - 1 - 2\,\ln\left(\sqrt{\det \mathbf{C}_e}\right) \tag{3}$$

$$\bar{\psi}_{kin} = \frac{c}{2}\,(\operatorname{tr}\mathbf{C}_{p_e} - 3) - c\,\ln\left(\sqrt{\det \mathbf{C}_{p_e}}\right) \tag{4}$$

$$\bar{\psi}_{iso} = Q\,(\kappa + \frac{e^{-\beta\,\kappa}}{\beta}) \tag{5}$$

are the parts of the Helmholtz free energy corresponding to the undamaged state. Note that due to the Neo-Hookean form of $\bar{\psi}_e$ the material model is capable of describing finite elastic strains. Here μ and Λ refer to the Lamé constants and c is the stiffness-like kinematic hardening parameter. The expression for $\bar{\psi}_{iso}$ corresponds to the saturation-type isotropic hardening rule of Voce [5] where Q and β are the isotropic hardening parameters. The relation for the second Piola-Kirchhoff stress tensor $\mathbf{S} = 2\,\mathbf{F}_p^{-1}\,(\partial\psi_e/\partial\mathbf{C}_e)\,\mathbf{F}_p^{-T}$ is obtained by making use of standard arguments [6].

The numerical implementation of the model is carried out in the reference configuration. The constitutive equations obtained from the thermodynamically consistent derivation are summarized below:

- Stress tensors

$$\mathbf{S} = (1-D)\left(\mu\,(\mathbf{C}_p^{-1} - \mathbf{C}^{-1}) + \frac{\Lambda}{2}\,(\det\mathbf{C}\,(\det\mathbf{C}_p)^{-1} - 1)\,\mathbf{C}^{-1}\right) \tag{6}$$

$$\bar{\mathbf{S}} = \frac{1}{1-D}\,\mathbf{S} \tag{7}$$

$$\mathbf{X} = c\,(\mathbf{C}_{p_i}^{-1} - \mathbf{C}_p^{-1}) \tag{8}$$

$$\mathbf{Y} = \mathbf{C}\,\bar{\mathbf{S}} - \mathbf{C}_p\,\mathbf{X}, \quad \mathbf{Y}_{kin} = \mathbf{C}_p\,\mathbf{X} \tag{9}$$

- Evolution equations

$$\dot{\mathbf{C}}_p = \dot{\lambda}\,\frac{\mathrm{sym}\Big(\mathbf{C}_p\left(\mathcal{A}\left[(\mathbf{Y}^D)^T\right]+(\mathcal{A}^T\left[\mathbf{Y}^D\right])^T\right)^D\Big)}{\sqrt{\mathbf{Y}^D\cdot(\mathcal{A}\left[(\mathbf{Y}^D)^T\right])}} \tag{10}$$

$$\dot{\mathbf{C}}_{p_i} = 2\,\dot{\lambda}\,\frac{b}{c}\,\mathbf{Y}^D_{kin}\,\mathbf{C}_{p_i},\quad \dot{\kappa}=\sqrt{\frac{2}{3}}\,\dot{\lambda} \tag{11}$$

$$\dot{D} = \dot{\lambda}\sqrt{\frac{2}{3}}\,\frac{1}{1-D}\left(\frac{Y}{s}\right)^k H(\kappa-p_D) \tag{12}$$

- Yield function

$$\Phi=\sqrt{\mathbf{Y}^D\cdot(\mathcal{A}\left[(\mathbf{Y}^D)^T\right])}-\sqrt{\frac{2}{3}}\left(\sigma_{y0}+Q\left(1-e^{-\beta\,\kappa}\right)\right) \tag{13}$$

- Fourth-order anisotropy tensor

$$\begin{aligned}\mathcal{A} &= a_1\,\mathcal{I}+a_2\,\mathbf{M}_1\otimes\mathbf{M}_1+a_3\,\mathbf{M}_2\otimes\mathbf{M}_2+a_4\left(\mathbf{M}_1\otimes\mathbf{M}_2+\mathbf{M}_2\otimes\mathbf{M}_1\right) \quad (14)\\ &+ a_5\,\mathcal{D}_1+a_6\,\mathcal{D}_2\\ D^\alpha_{ijkl} &= \frac{1}{2}\left(M^\alpha_{ik}\delta_{jl}+M^\alpha_{jl}\delta_{ik}+M^\alpha_{il}\delta_{jk}+M^\alpha_{jk}\delta_{il}\right),\quad \alpha=1,2 \quad (15)\\ \mathbf{M}_i &= \mathbf{N}_i\otimes\mathbf{N}_i,\quad i=1,2 \quad (16)\end{aligned}$$

- Kuhn-Tucker conditions

$$\dot{\lambda}\geq 0,\quad \Phi\leq 0,\quad \dot{\lambda}\,\Phi=0 \tag{17}$$

Here, $\mathbf{C}_p=\mathbf{F}_p^T\,\mathbf{F}_p$ and $\mathbf{C}_{p_i}=\mathbf{F}_{p_i}^T\,\mathbf{F}_{p_i}$ are right Cauchy-Green deformation-like tensors, $\mathbf{X}$ is the back stress tensor in the reference configuration, $\mathbf{Y}$ (not to be confused with the scalar quantity Y thermodynamically conjugate to D) and $\mathbf{Y}_{kin}$ represent non-symmetric second-order stress tensors. $\mathcal{A}$ is the fourth-order orthotropy tensor in the reference configuration written in terms of the second-order structure tensors $\mathbf{M}_1$ and $\mathbf{M}_2$. $\mathbf{N}_1$ and $\mathbf{N}_2$ are the privileged directions of the material in the reference configuration. The pre-factors a_i $(i=1,...,6)$ can be determined based on the classical Hill coefficients as elaborated in [7].

The evolution of the isotropic damage variable in (12) is applied following the work of Lemaitre [4]. Here, s and k are two positive material parameters describing the rate at which damage evolves. The Heaviside step function $H(\kappa-p_D)$ with properties $H=0$ if $\kappa<p_D$ and $H=1$ if $\kappa\geq p_D$ is utilized here to describe the threshold p_D where damage begins to evolve. The scalar Y is defined in [8] as the energy density release rate and is given here as

$$Y = \frac{R_\nu}{2E}\,\mathbf{Y}^D \cdot (\mathcal{A}\,[(\mathbf{Y}^D)^T]) \tag{18}$$

where R_ν is the so-called triaxiality function:

$$R_\nu = \frac{2}{3}(1+\nu) + 3(1-2\nu)\left(\frac{1/3\,\mathrm{tr}\,\mathbf{Y}}{\sqrt{\mathbf{Y}^D \cdot (\mathcal{A}\,[(\mathbf{Y}^D)^T])}}\right)^2 \tag{19}$$

In (18), $E = \mu(3\Lambda + 2\mu)/(\Lambda + \mu)$ represents Young's modulus of elasticity and $\nu = \Lambda/2(\Lambda + \mu)$ the Poisson's ratio.

The coupling between the anisotropic elastoplastic model and the Lemaitre-type isotropic damage model is carried out according to the effective stress concept: $\bar{\mathbf{S}} = 1/(1 - D)\,\mathbf{S}$. $\bar{\mathbf{S}}$ is the local effective stress which increases as damage develops in the material. Further, the stress tensor $\mathbf{Y}$ that appears in the yield function (13) depends on the effective stress $\bar{\mathbf{S}}$. Through the yield function and the plastic flow rule the plastic deformation as well as the hardening internal variables are also affected by the damage development in the material. In this way, a coupled framework of finite strain anisotropic damage-elastoplasticity is obtained, where the damage behaviour strongly depends on the anisotropically evolving plasticity in the material. Thus, the damage evolution shows induced anisotropy although from the mathematical point of view the damage formulation is isotropic.

The internal variables of the coupled damage-plasticity model are $\mathbf{C}_p$, $\mathbf{C}_{p_i}$, κ and D which describe the evolution of plastic deformation, kinematic hardening, isotropic hardening and damage, respectively. The tensor-valued evolution equations are discretized by a type of the exponential map algorithm (see [9]) that satisfies plastic incompressibility and uses the spectral decomposition to evaluate the exponential tensor functions in closed form. The discretization of the scalar evolution equations for κ and D is performed by the classical implicit backward Euler scheme.

3 THE NAKAJIMA STRETCHING TEST

This section discusses the application of the coupled damage-elastoplasticity model to simulate the so-called Nakajima test where six specimens are used to obtain six distinct points of the FLDF. The test represents a stretching operation up to fracture used to experimentally determine forming limit diagrams. The tools used in the Nakajima test include a hemispherical punch, a blankholder (Fig. 1(a)) and a die (Fig. 1(b)). For the simulation, six different blank specimens with varying width of the middle section (15, 25, 35, 45, 55 and 100 mm) are created. The corresponding Nakajima tests are performed for each specimen. The major and minor strains recorded at the end of each of these simulations correspond to a point on the FLDF. The specimens with widths of 15, 45 and 100 mm correspond essentially to strain states of uniaxial, plane and biaxial tension,

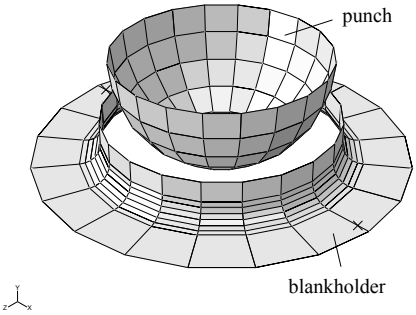

(a) Punch and blank holder.

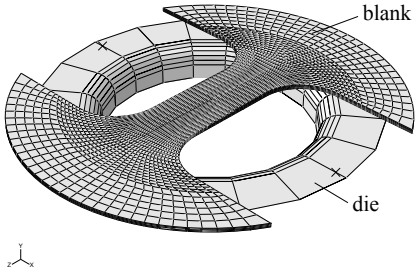

(b) Die and undeformed blank.

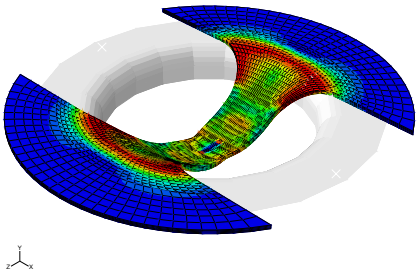

(c) Die and deformed blank.

Figure 1: Tools for the Nakajima test.

respectively. The specimen with a width of 15 mmm is depicted in Fig. 1(b) and in Fig. 1(c) in the undeformed and deformed configuration, respectively.

The material degradation in the element where failure occurs can be seen from the stress-strain curves up to fracture in Fig. 2. The corresponding evolution of the damage variable are shown in Fig. 3. Contour plots in Fig. 4(a) to Fig. 4(f) shows the bottom view distribution of damage for each specimen.

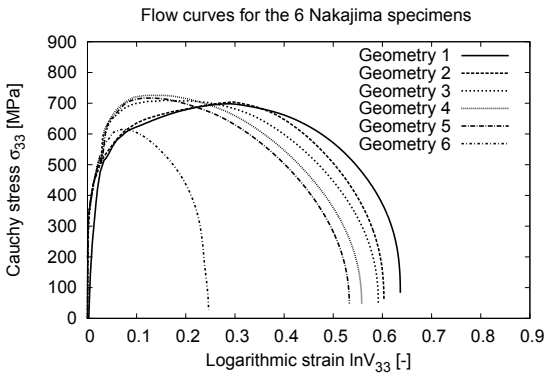

Figure 2: Flow curves - specimens 1 to 6.

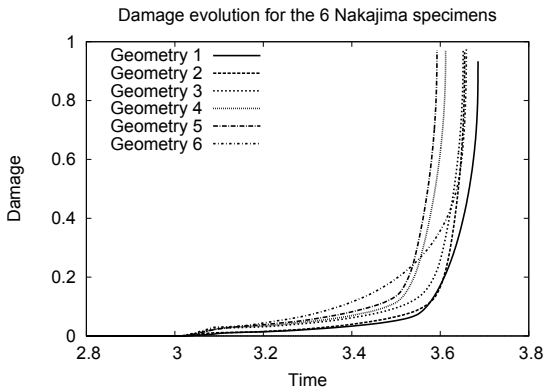

Figure 3: Damage evolution - specimens 1 to 6.

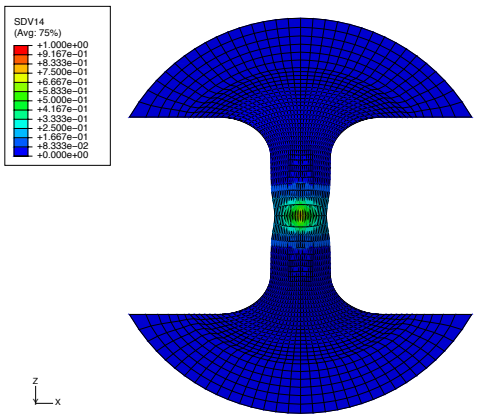

(a) Geometry 1, width 15 mm.

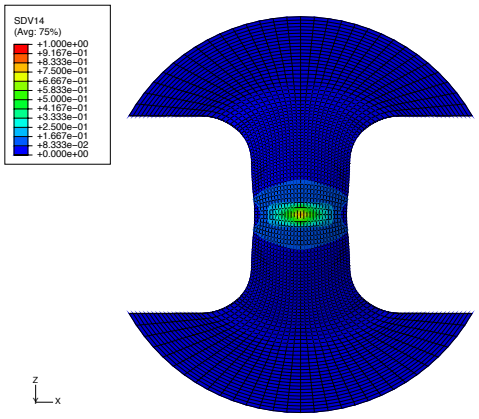

(b) Geometry 2, width 25 mm.

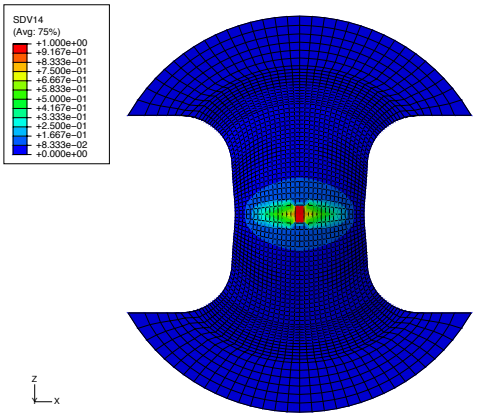

(c) Geometry 3, width 35 mm.

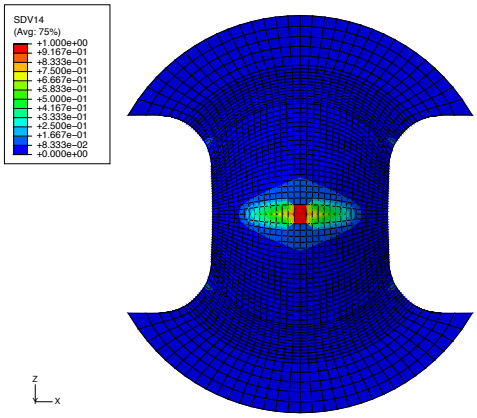

(d) Geometry 4, width 45 mm.

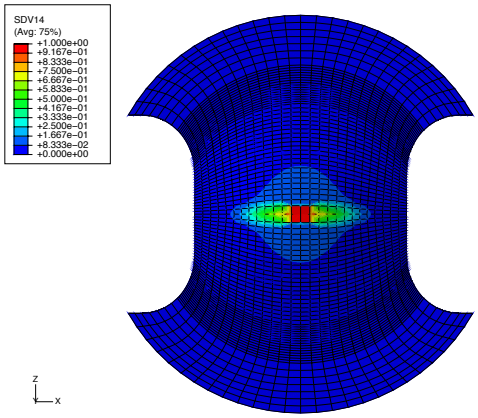

(e) Geometry 5, width 55 mm.

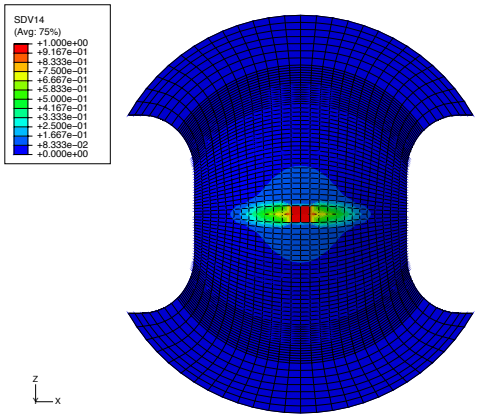

(f) Geometry 6, width 100 mm.

Figure 4: Damage distribution from the six Nakajima test specimens.

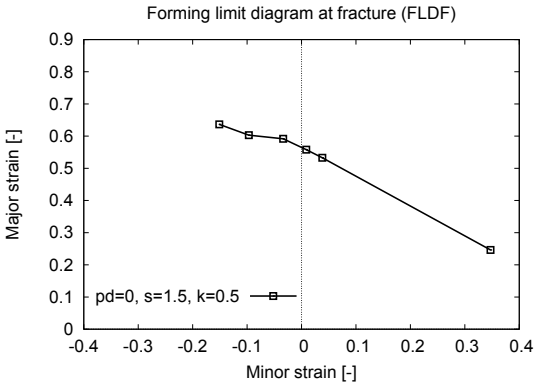

Figure 5: FLDF obtained by Nakajima tests.

Finally, the FLDF can be constructed by recording the major and minor strains for the ruptured element and by plotting them as points in the limit strain space. The six Nakajima test simulations give six combinations of major and minor strains ranging from uniaxial tension to biaxial tension. The FLDF is shown in Fig. 5. The major strain is 0.246 whereas the minor strain is 0.347. It is worth noting, that this difference occurs due to the considered plastic anisotropy in the FE computations.

4 THERMOMECHANICAL ANALYSES OF A ROCKET COMBUSTION CHAMBER SEGMENT

This section discusses the application of the presented model for the lifetime prediction of a rocket combustion chamber segment. Fig. 6(a) shows a typical rocket combustion chamber. The schematic cross section of the chamber is shown in Fig. 6(b). The outer wall is made out of nickel alloy. The cooling channel walls are made out of copper alloy. The hot gas resulting from the combustion of the propellants (liquid oxygen and liquid hyrogen) flows through the center of the chamber. The coolant (liquid hydrogen) flows through the small cooling channel passages. There can be up to 360 cooling channels in the circumference direction. The geometry of the modelled segment is the quasi Vulcain geometry following the work of Kuhl et al. [10]. First of all, a transient thermal analysis of the combustion chamber segment is performed to obtain the temperature field of the entire chamber segment. The obtained temperature history is then used as input for the user subroutine in the static analyses.

4.1 Transient heat transfer analysis

Convective thermal boundary conditions are employed at the inner and outer radii as well as in the cooling channel similar to the work of Riccius et al. [11]. The left and right sides have zero flux boundary conditions to ensure symmetry of the thermal field. The thermal cycle described in Table 1 is applied in the analysis. Fig. 7 shows some snapshots of the temperature field resulting from the transient thermal analysis.

4.2 Static analyses

The goal of the static analysis is to see the feasibility of the implemented damage model to describe the dog-house failure mode qualitatively. The pressure cycle in Table 2 is applied as load in the static analyses. For the static analyses 8-node brick elements

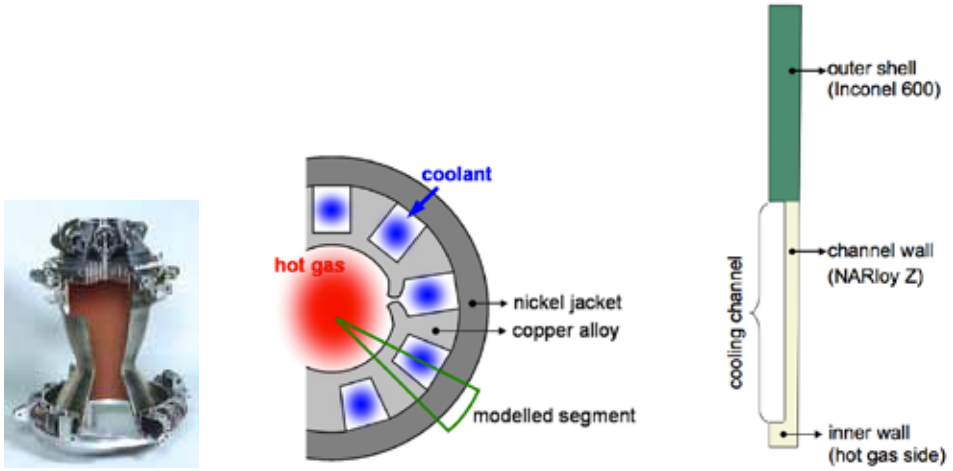

(a) A typical rocket combustion chamber.

(b) A schematic cross section of a typical rocket combustion chamber.

(c) Modelled segment of the quasi Vulcain thrust chamber at the throat.

Figure 6: Schematic cross section of a typical rocket combustion chamber and the modelled segment.

Phase	Time [s]	T_{hotgas} [K]	$T_{coolant}$ [K]
Pre-cooling	0 - 2	40	40
Hot run	3 - 603	950	40
Post-cooling	604 - 605	40	40
Relaxation	605 - 620	293.15	-

Table 1: Thermal cycle applied for the transient thermal analysis.

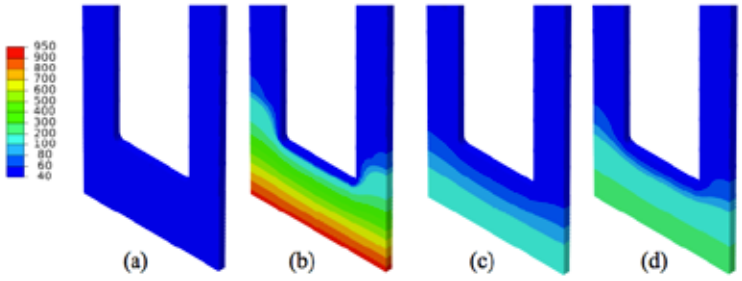

Figure 7: Temperature distribution at different phases of the assumed operational cycle: (a) pre cooling (b) hot run (c) post cooling (d) relaxation.

with reduced integration were applied. The critical area of interest is the cooling channel wall at the hot gas side. Two different meshes were used. The coarser and the finer mesh

Phase	Time [s]	P_{hotgas} [MPa]	$P_{coolant}$ [MPa]
Pre-cooling	0 - 2	0	2
Hot run	3 - 603	10	14.5
Post-cooling	604 - 605	0	2
Relaxation	605 - 620	0	0

Table 2: Pressure cycle applied for the static analyses.

have in total 1338 and 4014 elements respectively. Fig. 8 shows the discretization of the hot gas side wall using both meshes. The corner of the cooling channel passage is rounded with 0.1 mm fillet radius.

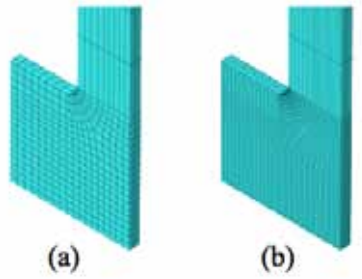

Figure 8: (a) Mesh 1 with 1338 elements. (b) Mesh 2 with 4014 elements.

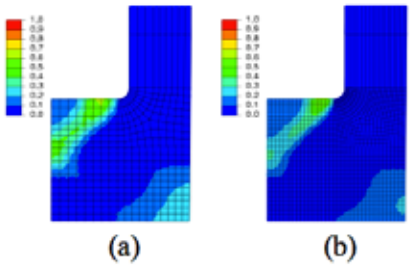

Figure 9: Damage distribution obtained from the static analyses: (a) Mesh 1 at the 16th cycle. (b) Mesh 2 at the 13th cycle.

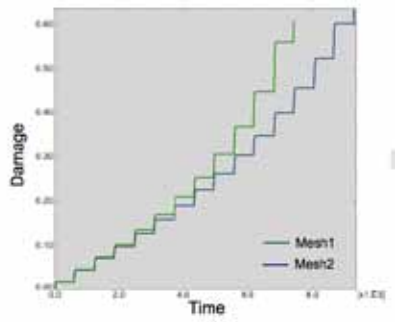

Figure 10: The cyclic evolution of the damage over time.

The damage distribution obtained from the analyses are shown in Fig. 9. The computation using Mesh 1 could be performed up to 16 cycles. Applying Mesh 2 the computation could be performed up to 13 cycles. As the damage increases, the local iteration within the user subroutine requires smaller and smaller time steps. The corresponding cyclic damage evolutions over time are shown in Fig. 10. Here it can be seen that with the coarser mesh, the damage evolves slightly faster, in comparison to the one obtained using the finer mesh.

This indicates a mesh dependency of the result. On the one hand this phenomenon could be attributed to the well-known localization effect in elastoplasticity coupled with damage. Another possible explanation is that simply the mesh is still too coarse to yield a converged result. An investigation which clarifies these issues is under way. In any case, improvement of the robustness of the computation shall enable the computation of more

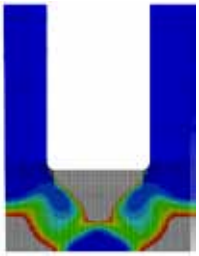

(a) Predicted end shape of the cooling channel segment.

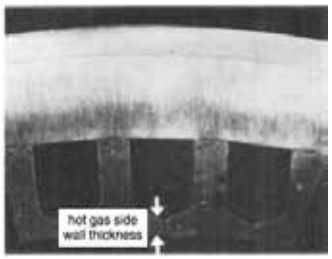

(b) The dog-house failure mode occured in a NARloy-Z thrust chamber [12].

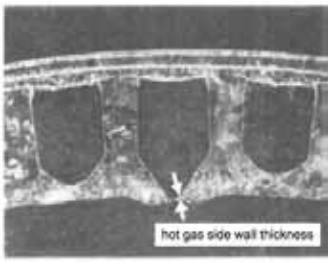

(c) The dog-house failure mode occured in an OFHC thrust chamber [12].

Figure 11: The predicted end shape of the channel segment from the simulation and the dog-house failure mode.

loading cycles. It is important to eliminate the convergence problem in the solution of the time discretized equation system to determine the internal variables. Fig. 11(a) shows the predicted end shape of the cooling channel segment. The grey area represents the area mostly affected by damage. Fig. 11(b) and Fig. 11(c) show cross sections of combustion chambers made out of NARloy-Z copper alloy and OFHC (oxygen free copper) alloy respectively. It is concluded by Hannum et al. [12] that depending on the liner material, the causes of the failure are different. In a NARloy-Z combustion chamber, the hot gas side wall does not bulge so much towards the chamber. Failure is then caused by low cycle fatigue. In an OFHC combustion chamber, the wall becomes significantly thinner. Cracking occurs after a necking phenomenon.

5 CONCLUSIONS

The coupling of a finite anisotropic elastoplastic model with isotropic ductile damage has been presented. The implementation of the model for finite element simulations in two challenging applications has shown the good potential of the model for failure prediction purposes.

6 ACKNOWLEDGEMENTS

The authors gratefully acknowledge the support provided by the German Science Foundation within the projects TP3 of the PAK343 "Methods for quasistatic-dynamic combined forming processes" and TP D3 of the CRC/Transregio 40 "Fundamental Technologies for the Development of Future Space-Transport-System Components under High Thermal and Mechanical Loads".

References

[1] I. N. Vladimirov, M. P. Pietryga, and S. Reese. Anisotropic finite elastoplasticity with nonlinear kinematic and isotropic hardening and application to sheet metal forming. *International Journal of Plasticity*, 26:659–687, 2010.

[2] C. O. Frederick and P. J. Armstrong. A mathematical representation of the multiaxial bauschinger effect. *Materials at High Temperatures*, 24:1–26, 2007.

[3] Jr. Daniel T. Butler and Marek-Jerzy Pindera. Analysis of factors affecting the performance of rlv thrust cell liners. Technical report, NASA Glenn Research Center, 2004.

[4] J. Lemaitre. *A Course on Damage Mechanics*. Springer, Berlin, 1992.

[5] E. Voce. The relationship between stress and strain for homogeneous deformation. *Journal of Institute of Metals*, 74:537–562, 1948.

[6] B. D. Colemann and M. Gurtin. Thermodynamics with internal variables. *Journal of Chemical Physics*, 47(597–613), 1967.

[7] I. N. Vladimirov, M. P. Pietryga, and S. Reese. On the influence of kinematic hardening on plastic anisotropy in the context of finite strain plasticity. *International Journal of Material Forming*, 2011.

[8] J. Lemaitre and J. L. Chaboche. *Mechanics of Solid Materials*. Cambridge University Press, Cambridge, 1995.

[9] I. N. Vladimirov, M. P. Pietryga, and S. Reese. On the modeling of nonlinear kinematic hardening at finite strains with application to springback - comparison of time integration algorithms. *International Journal of Numerical Methods in Engineering*, 75:1–28, 2008.

[10] D. Kuhl, Jörg Riccius, and O.J. Haidn. Thermomechanical analysis and optimization of cryogenic liquid rocket engines. *Journal of Propulsion and Power*, 18:835–846, 2002.

[11] Jörg R. Riccius and E. B. Zametaev. Stationary and dynamic thermal analyses of cryogenic liquid rocket combustion chamber walls. In *38th AIAA/ASME/SAE/ASEE Joint Propulsion Conference and Exhibit*, 2002.

[12] Ned P. Hannum and Jr. Harold G.P̃rice. Some effects of thermal-cycle-induced deformation in rocket thrust chambers. Technical report, NASA Langley Research Center, April 1981.